

ARTICLE OPEN

Structural role of ZrO₂ and its impact on properties of boroaluminosilicate nuclear waste glassesXiaonan Lu¹, Lu Deng¹, Sebastien Kerisit² and Jincheng Du¹ 

Addition of zirconia (ZrO₂) to nuclear waste glasses, even in small amount, significantly affects physical properties such as chemical durability, density, viscosity, and glass transition temperature. Hence ZrO₂ plays an important role in the development of nuclear waste glass compositions. It was found recently that addition of zirconia decreases the initial dissolution rate but increases long-term dissolution by changing the protective properties such as porosity of alteration layers. In this study, the International Simple Glass (ISG) with different amounts of ZrO₂/SiO₂ substitution was simulated using classical molecular dynamics (MD) simulations and recently developed composition-dependent potential sets. Local structural descriptors such as bond distances, bond angle distributions, and coordination numbers were systematically studied and compared with experimental values. Zr K-edge extended X-ray absorption fine structure spectra were also calculated and compared with experiment to resolve the local coordination environment around Zr. Medium-range structural information (e.g., Q_n distribution, network connectivity, and ring-size distribution) showed that ZrO₂/SiO₂ substitution increases the overall network connectivity and the amount of smaller sized rings, which will decrease the initial dissolution rate by strengthening the glass network and limiting water diffusivity. Finally, diffusion and dynamic properties of the ions were studied and discussed to develop a better understanding of the chemical durability of these glasses.

npj Materials Degradation (2018)2:19; doi:10.1038/s41529-018-0041-6

INTRODUCTION

Borosilicate glasses have been used as one of the vitrification materials of radioactive wastes in many countries.¹ International Simple Glass (ISG) is a simplified model composition for a collaborative study of dissolution/corrosion mechanism of high-level waste (HLW) glasses.^{2–4} ISG has been intensively researched recently with studies focusing on its dissolution behavior under different conditions,^{3,5–12} its surface quality,¹³ radiation effect,^{14–18} waste loading,¹⁹ mechanical property,^{20,21} and especially on the properties of its alteration layers using diverse techniques such as electron microprobe analysis,²² Doppler broadening positron annihilation spectroscopy,²³ and atom probe tomography.²⁴

However, due to the lack of long-range periodicity, the structural study of glass materials exhibits many challenges. Detailed information of glass structure provides better understanding of glass physical properties and chemical durability, which helps design glass compositions for different waste types and geological disposals. Molecular dynamics (MD) simulation is an effective method of studying structural information in glass materials, and it provides a direct observation of atomic structure, which is difficult to obtain from experimental methods.²⁵ Many studies have been systematically conducted and revealed short-range and medium-range structural features utilizing MD simulation in various glass systems such as sodium silicate glasses,²⁶ aluminosilicate glasses,²⁷ lithium disilicate glasses,²⁸ cerium aluminophosphate glasses,²⁹ europium-doped silicate glasses,^{30,31} erbium-doped sodium silicate glasses,³² lithium vanadophosphate glasses,³³ and bioactive glasses.^{34–36} However, MD simulation of nuclear waste glasses has been limited due to the

lack of pairwise potential sets for boron. With the recent development of modified composition-dependent pairwise potential sets, it is now possible to simulate complex glass compositions.^{36,37} ISG was successfully simulated with MD,³⁷ structural related properties such as the percentage of 4-coordinated boron, PDFs, bond angle distributions (BADs) and ring-size analysis, were calculated and found to be in agreement with available experimental data.

Even though zirconia content is low in ISG, it is essential to study the local environment of zirconia in ISG and the effect of ZrO₂/SiO₂ substitution for the benefit of glass formulation. Indeed, addition of ZrO₂ has been found to significantly alter the physical properties of alkali silicate glasses, such as increase the density, viscosity, glass transition temperature, and decrease the thermal expansion coefficient.^{38,39} ZrO₂ has been reported to enhance the chemical durability of glasses not only in neutral pH condition but also in alkali-rich environments.^{38–40} However, even though the initial dissolution rate drops significantly with increasing ZrO₂ concentration (up to 8 mol%) in soda-lime borosilicate glasses, recent findings showed that the inhibiting effect of ZrO₂ on the dynamics of alteration layer formation ultimately results in a greater degree of corrosion in the long term.^{41–43} Zirconium ions were found to be mostly six-fold coordinated and [ZrO₆] octahedra link with other network formers such as [SiO₄] tetrahedra through corner-sharing.^{44–46} This feature was also observed in MD simulations of a 42CaO-48SiO₂-10ZrO₂ glass⁴⁷ and a sodium alumina borosilicate glass.⁴⁶ Moreover, MD simulations revealed that amorphization of crystalline zircon (ZrSiO₄) leads to polymerization of the silicon-oxygen network.⁴⁸ Similarly, addition of ZrO₂ was found to polymerized glass network in sodium-lithium borosilicate glasses by attracting

¹Department of Materials Science and Engineering, University of North Texas, Denton, TX 76203, USA and ²Physical and Computational Sciences Directorate, Pacific Northwest National Laboratory, Richland, WA 99352, USA
Correspondence: Jincheng Du (Du@unt.edu)

Received: 15 January 2018 Revised: 25 April 2018 Accepted: 10 May 2018
Published online: 22 June 2018

alkali cations to charge compensate six-fold coordinated zirconium ion.⁴⁹ However, very few studies investigate the structural changes altered by ZrO₂ concentration in boron-containing nuclear waste glasses and its relationship between glass structure and dissolution behaviors by using MD simulations.

Therefore, the purposes of this study are to systematically study with MD simulations the structural and dynamical changes of ISG upon ZrO₂/SiO₂ substitution. Specifically, the local environment of cations and medium-range structural information are computed, including the Zr K-edge extended X-ray absorption fine structure

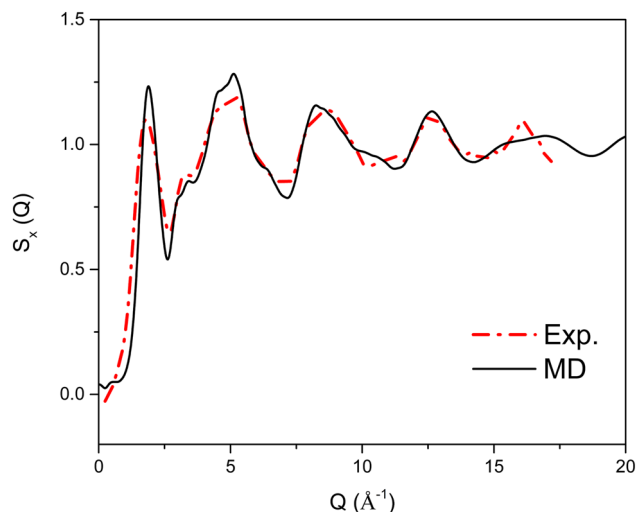


Fig. 1 Comparison of X-ray diffraction structure factors of 2Zr (ISG) obtained from experiment⁵⁷ and MD simulation

(EXAFS) spectrum, and the changes caused by ZrO₂/SiO₂ substitution are discussed in terms of their effect on dissolution.

RESULTS

General structural information

To validate our MD simulation results, a comparison of X-ray structure factors of 2Zr (ISG) obtained from experiment and MD simulation is shown in Fig. 1. The calculated structure factor is in good agreement with the experimental data, indicating an overall reasonable structure model generated from our MD simulation. The peak position of the first four peaks and the shoulder of the second peak are matched between experiment and MD simulation, except that the first two peaks from MD simulation have slightly higher intensities. There are small differences on the third valley and the fifth peak, which provide direction for future potential improvement.

Selected bond lengths of simulated 0Zr, 2Zr (ISG), 3Zr, and 4Zr glasses obtained from the first peak of pair distribution functions (PDFs) and comparison with values found in literature are listed in Table 1, and plots of PDFs of 4Zr glass are shown in Fig. 2. Bond length of Si-O is 1.61 Å regardless of composition, which is in excellent agreement with experimental values for glasses with or without zirconium.^{26,47,50} The two peaks observed for all compositions in the B-O PDFs are due to ^[3]B-O and ^[4]B-O bond lengths centered around ~1.46 Å and ~1.55 Å, respectively. Bond lengths of Al-O and Zr-O are ~1.77 Å and ~2.10 Å, respectively, and are also consistent with experimental values (see Table 2).⁵¹⁻⁵⁵ Bond lengths of Zr with other cations are also in line with values found in the literature, although slight differences might be caused by different compositions and characterization methods. No noticeable changes were observed for bond lengths of

Table 1. Selected bond lengths (Å) in simulated 0Zr, 2Zr (ISG), 3Zr, and 4Zr glasses and comparison with literature values

Bond distance (Å)	0Zr		2Zr (ISG)	3Zr	4Zr	ZrO ₂ added
	MD	Ref.				
Si-O	1.62 ± 0.01	1.62 ^a	1.61	1.61	1.61	1.6 ^b
^[3] B-O	1.45	1.48 ^c	1.45 ± 0.01	1.46	1.46	1.40 ^d
^[4] B-O	1.54	1.48 ^c	1.55	1.55	1.55	1.60 ^d
Na-O	2.46 ± 0.01	2.36 ^a	2.47 ± 0.01	2.47 ± 0.01	2.47 ± 0.01	2.22–2.55 ^e
Ca-O	2.41 ± 0.02	2.31 ^f	2.42 ± 0.01	2.44 ± 0.01	2.42 ± 0.02	2.4 ^b
Al-O	1.77 ± 0.01	1.76 ^g	1.78	1.78	1.78	
Zr-O	–		2.10 ± 0.01	2.11	2.10 ± 0.01	~2.09 ^{h-1} , 2.14 ^b
Zr-Al	–		3.62 ± 0.09	3.50 ± 0.03	3.59 ± 0.02	
Zr-Si	–		3.56 ± 0.02	3.55 ± 0.01	3.55 ± 0.01	3.39 ^h , 3.42 ^j , 3.5 ⁱ , ~3.66 ^k
Zr-B	–		3.41 ± 0.02	3.42 ± 0.03	3.40 ± 0.02	~3.5 ^k
Zr-Na	–		3.42 ± 0.04	3.46 ± 0.01	3.42 ± 0.04	3.44 ^j , 3.65 ^k
Zr-Ca	–		3.40 ± 0.09	3.48 ± 0.07	3.46 ± 0.03	3.56 ^b
Zr-Zr	–		3.42 ± 0.46	3.54 ± 0.36	3.56 ± 0.30	3.4 ^b , 3.7 ⁱ

Standard deviations were obtained from three parallel tests and numbers without errors have a standard deviation less than 0.005

^aNeutron diffraction (ND) of silicate glasses, see summary in^{26,50}

^bCrystalline values for Si-O and Ca-O, EXAFS value for Zr-O of a 42CaO-48SiO₂-10ZrO₂ glass, see summary in⁴⁷

^cB-O distance from ND of alkali/alkaline-earth borosilicate glasses⁷⁴

^dND in combination with reverse Monte Carlo (RMC) of (65-x)SiO₂-xB₂O₃-25Na₂O-5BaO-5ZrO₂, x = 5–15 mol% glasses⁷⁵

^eWide-angle X-ray scattering in combination with RMC of sodium (alumino) borosilicate glasses containing small amount of ZrO₂⁷⁶

^fND/RMC of Bioglass⁷⁷

^gND of aluminosilicate glasses⁷⁸

^hEXAFS of French models of inactive nuclear waste glasses⁴⁴

ⁱX-ray diffraction of a 57CaO-37SiO₂-6ZrO₂ glass⁷⁹

^jEXAFS of zirconium added alkali borosilicate waste glasses⁶⁰

^kEXAFS of soda-lime borosilicate glasses⁵⁸

^lEXAFS of high zirconia borosilicate glasses⁸⁰

cation–oxygen and cation–cation pairs between compositions. BADs of oxygen–cation–oxygen and coordination number of cation–oxygen pairs are not sensitive to ZrO₂/SiO₂ substitution, and details can be found in supplementary information.

Preference of modifiers around glass network formers oxygen polyhedra

To further investigate the distribution of modifiers around each network former, CNs of Na and Ca around Si, Al, Zr, B, ^{[3]B}, and ^{[4]B} were analyzed and all values can be found in supplementary information. The number of Ca ions around each former is lower than that of Na due to the higher content of Na in each glass composition. In order to eliminate these compositional effects, preferential distributions of modifier cations around glass former cations were calculated according to a study by Tilocca et al.,⁵⁶

$$R_{Na/Ca}^{Former} = \frac{CN_{former-Na}}{CN_{former-Ca}} \times \frac{N_{Ca}}{N_{Na}} \quad (1)$$

where N is the number of modifier cations present. Preferential distributions for Na and Ca around Si, B, ^{[3]B}, ^{[4]B}, Al, and Zr in simulated 0Zr, 2Zr, 3Zr, and 4Zr glasses are shown in Table 3. A ratio of $R > 1$ indicates the preference for Na, and vice versa. As shown in Table 3, Si has higher preference of Na than Ca, while Zr has a slightly higher preference for Ca. No preference for Al in 0Zr was observed considering the standard deviations, while Al prefers Ca in glasses containing Zr. ^{[4]B} prefers Ca for all compositions, while more Na ions were found around ^{[3]B}.

Medium-range structural information

Network connectivity values calculated from Q_n distribution of Si, B, Zr, Al and overall NC in simulated 0Zr, 2Zr, 3Zr, and 4Zr glasses

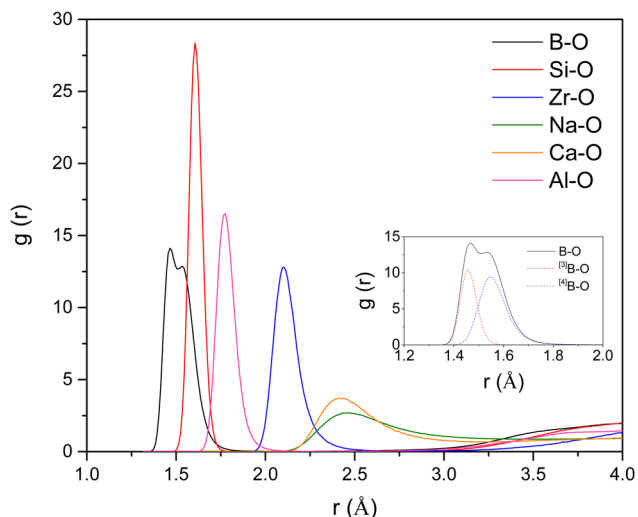


Fig. 2 Pair distribution functions (PDFs) of cation–oxygen pairs in simulated 4Zr glass. The inset shows PDF of B–O, ^{[3]B}–O and ^{[4]B}–O pairs

are listed in Table 4. Detailed Q_n distribution of Si, B, Zr and Al, and percentages of non-bridging oxygen (NBO), bridging oxygen (BO) and tri-bridging oxygen (TBO) cluster in simulated 0Zr, 2Zr, 3Zr, and 4Zr glasses can be found in supplementary information. Overall, NC increases from 3.76 to 3.82 for 0Zr to 4Zr. Due to the high content of glass formers in these glass compositions, NCs of Si, B, Zr, and Al are similar with their coordination numbers, which indicates a well-connected network structure.

Polyhedral analysis was performed in order to study the linkages between network former polyhedra. Numbers of polyhedral linkages between network formers in simulated glasses can be found in supplementary information. Connections between [SiO₄]-[SiO₄], [AlO₄]-[SiO₄], and [BO₃]/[BO₃]-[SiO₄] are mostly (over 99.9%) corner-sharing for all compositions. There exist small amount of edge-sharing linkages (less than 4%) between [AlO₄]-[BO₄], [AlO₄]-[AlO₄], and [BO₄]-[BO₄] but the remaining majority (>96%) of these connections are corner sharing. No noticeable changes were observed between compositions among the linkages between Si, Al, and B polyhedra. Among all the linkages with Zr, [SiO₄]-[ZrO₆], [BO₄]/[BO₃]-[ZrO₆], and [AlO₄]-[ZrO₆] linkages change from 64.0 to 60.2%, 28.7 to 29.8% and 6.5 to 7.3% for 2Zr (ISG) to 4Zr, respectively, which is consistent with the contents of network-former atoms in each glass composition. Connections between [ZrO₆]-[ZrO₆] increases from ~1 to 3% for 2Zr to 4Zr. A few edge-sharing and face-sharing [ZrO₆]-[ZrO₆] linkages were observed with increasing Zr content. Due to the small amount of [ZrO₆]-[ZrO₆] connections (less than 0.4%) among all the linkages between network formers, no obvious clustering behavior was considered. Snapshots of the simulated 4Zr glass are presented in Fig. 3.

Ring-size distributions of simulated 0Zr, 2Zr, 3Zr, and 4Zr glasses are shown in Fig. 4. In the analysis, all the network former cations Si⁴⁺, B³⁺, Al³⁺, and Zr⁴⁺ were counted in the ring size analysis. Ring-size distributions of all glass compositions exhibit a Gaussian type of distribution but slightly tilted toward larger sized rings. The peak is located at seven-membered rings, indicating a well-connected three-dimensional random network. Average ring size for 0Zr, 2Zr, 3Zr, and 4Zr glasses is 7.54 ± 0.07 , 7.42 ± 0.02 , 7.32 ± 0.02 and 7.28 ± 0.02 , respectively. With addition of ZrO₂, the peak position of ring size distribution shifts toward smaller ring sizes

Table 2. Comparison of 4-coordinated B (N_4 , %) with different system sizes for simulated 0Zr, 2Zr, 3Zr, and 4Zr glasses

N_4 (%)	3000	6000	12,000	24,000	YDB model	NMR
0Zr	60.5 ± 1.0	58.2 ± 1.5	60.7 ± 0.7	60.1 ± 1.6	61.6	
2Zr (ISG)	58.5 ± 0.8	60.0 ± 0.7	59.4 ± 0.9	59.4 ± 0.3	62.3	52^{37} $\sim 58^{14}$
3Zr	59.5 ± 2.0	59.4 ± 1.7	59.8 ± 1.2	58.8 ± 1.4	61.1	
4Zr	60.5 ± 1.3	60.9 ± 0.7	60.0 ± 0.2	60.3 ± 0.1	60.7	

Standard deviation was obtained from three parallel tests

Table 3. Preferential distribution of Na/Ca around Si, B, ^{[3]B}, ^{[4]B}, Al, and Zr in simulated 0Zr, 2Zr, 3Zr, and 4Zr glasses

Na/Ca	R_{Si}	R_B	$R_{[3]B}$	$R_{[4]B}$	R_{Al}	R_{Zr}
0Zr	1.12 ± 0.02	0.97 ± 0.02	1.10 ± 0.05	0.92 ± 0.02	1.05 ± 0.06	–
2Zr (ISG)	1.13 ± 0.02	0.99 ± 0.03	1.14 ± 0.02	0.93 ± 0.04	0.94 ± 0.02	0.85 ± 0.15
3Zr	1.13 ± 0.02	0.97 ± 0.02	1.12 ± 0.05	0.90 ± 0.02	0.89 ± 0.05	0.99 ± 0.06
4Zr	1.15 ± 0.02	0.95 ± 0.02	1.13 ± 0.04	0.87 ± 0.01	0.94 ± 0.03	0.91 ± 0.07

Standard deviation was obtained from three parallel tests

and peak intensity increases, suggesting that a tightened glass network structure after ZrO₂/SiO₂ substitution.

Boron speciation and environments

Comparison of 4-coordinated B (N₄) with different system sizes (3000, 6000, 12,000, 24,000 atoms) for simulated 0Zr, 2Zr, 3Zr, and 4Zr glasses are listed in Table 2. N₄ values are consistent between various system sizes, where larger system sizes provide smaller standard deviations. N₄ values are in excellent agreement (less than 4% difference) with YDB model. N₄ of ISG (~60%) is slightly higher than NMR results (~52% or ~58%) from literature.^{14,37} Detailed CNs of Si, B, Al, and Zr around B in simulated 0Zr, 2Zr, 3Zr, and 4Zr glasses can be found in supplementary information.

From direct observation of glass structure, linkages of single ^{[3]B}/^{[4]B} surrounded by Si, Al or Zr were found and some representatives are shown in Fig. 5. Due to the different hydrolysis rate and reaction energy of various linkages in the glasses (e.g., Si–O–Si, Si–O–^{[4]B}, ^{[3]B}–O–^{[3]B}, etc.), these features might have an impact on the dissolution of glass and the small amount of retention of boron in alteration layers observed experimentally.³⁷ Detailed discussion can be found in Discussion section.

Zirconium environment and EXAFS calculations

The calculated Zr K-edge EXAFS spectrum for 2Zr (ISG) and its Fourier transform are compared to the room-temperature experimental data of Bouty et al.⁵⁷ in Fig. 6. The calculated spectra for 3Zr and 4Zr glasses were identical to that of 2Zr, as would be expected based on the structural analysis presented above. The agreement is good in terms of both the positions and

	NC _{Si}	NC _B	NC _{Zr}	NC _{Al}	NC _{overall}
0Zr	3.84 ± 0.01	3.54 ± 0.02	–	3.99 ± 0.01	3.76 ± 0.01
2Zr (ISG)	3.86	3.54	5.32 ± 0.03	3.99	3.79
3Zr	3.87 ± 0.01	3.53 ± 0.02	5.25 ± 0.03	3.98 ± 0.01	3.81 ± 0.01
4Zr	3.87	3.52	5.22 ± 0.01	3.98 ± 0.01	3.82

Standard deviation was obtained from three parallel tests and numbers without errors have a standard deviation less than 0.005

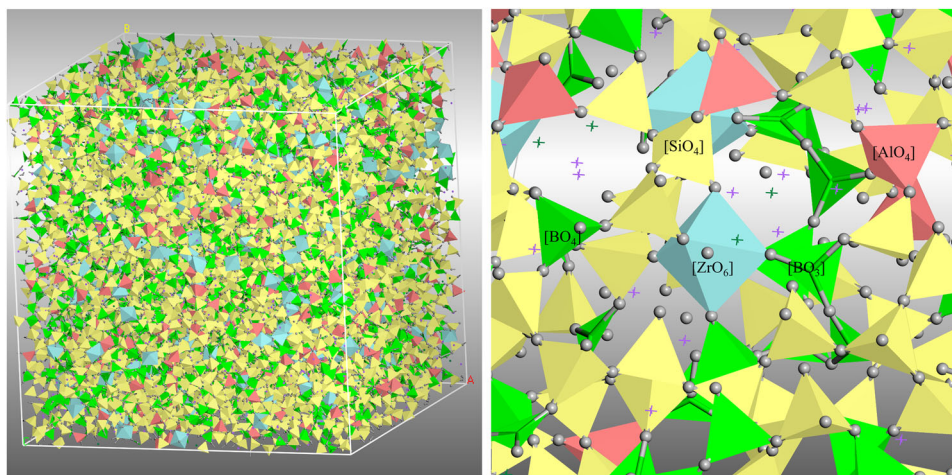


Fig. 3 Snapshots of simulated 4Zr: Zr, blue octahedra; Si, yellow tetrahedra; B, green triangles (^{[3]B}) and green tetrahedral (^{[4]B}); Al, red tetrahedral; O, small grey balls; Na, purple crosses; Ca, green crosses

amplitudes of the spectral features. As a result, a very good match to experiment is obtained for the FT magnitude of the first coordination shell. The peak at 0.86 Å in the FT of the experimental spectrum is assigned to noise as it was not present in the calculations or in the experimental Zr K-edge EXAFS spectra of other glasses with similar compositions,⁵⁸ was not included by Bouty et al.⁵⁷ in their fits, and does not correspond to any physically possible Zr–O distance.

Although the FT magnitude of the peaks between approximately 2.5 and 4 Å and corresponding to the second coordination shell is much lower than that of the first shell, the calculated peak positions and magnitudes are similar to those obtained from the FT of the experimental spectrum. Jollivet et al.⁵⁸ reported Zr K-edge EXAFS measurements for a series of four borosilicate glasses with varying amounts of CaO and ZrO₂ oxide components. The four glasses showed very similar spectra. The spectrum obtained for the glass labeled Z4C4 (56.7 mol% SiO₂, 17.9 mol% B₂O₃, 18.0 mol% Na₂O, 3.7 mol% CaO, 3.9 mol% ZrO₂), which had a similar composition to ISG, is also shown in Fig. 6. This spectrum is comparable to the ISG spectra, albeit with greater amplitudes as the measurements were made at 35 K to reduce the dampening effect of thermal disorder. The FT magnitude due to the second

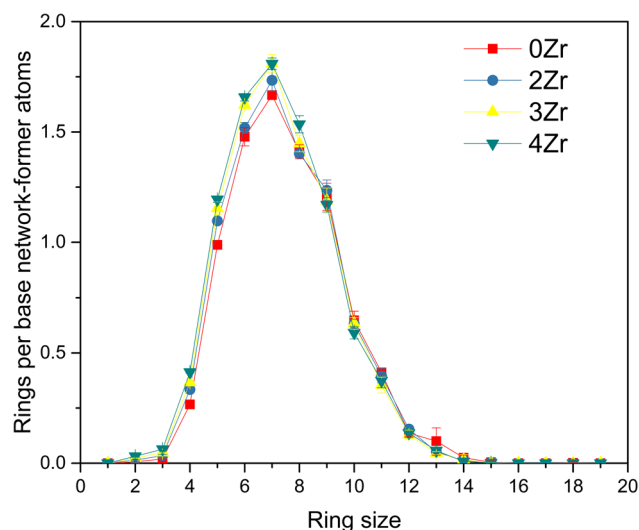


Fig. 4 Ring-size distributions of simulated 0Zr, 2Zr, 3Zr, and 4Zr glasses

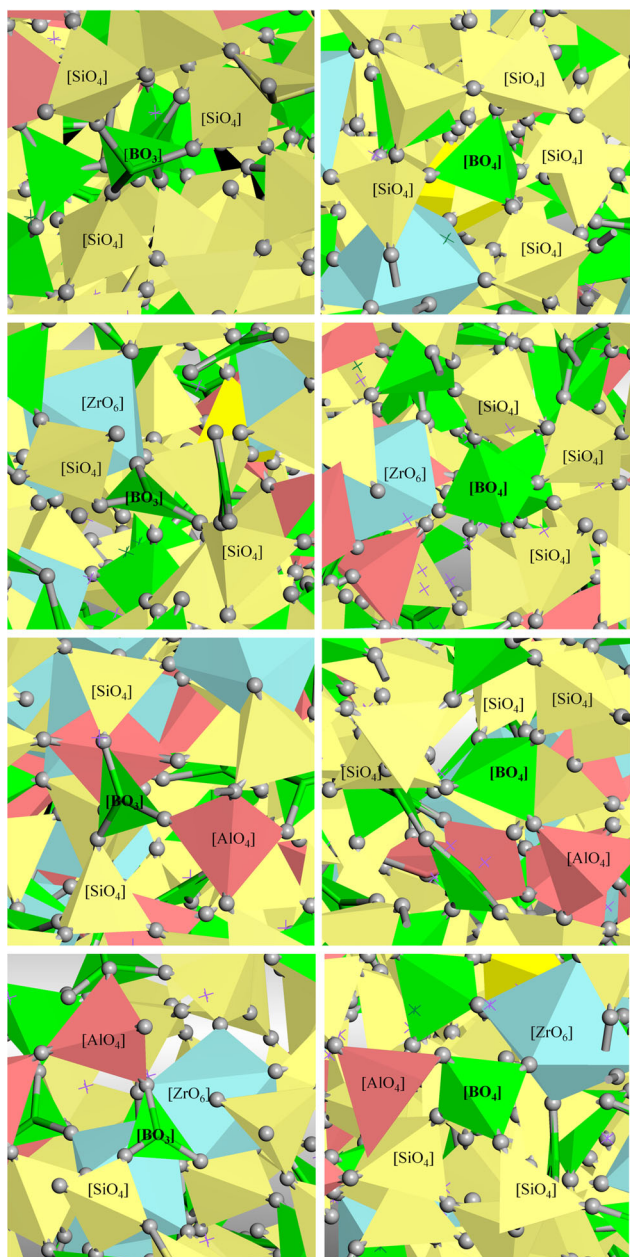


Fig. 5 Snapshots of simulated 4Zr glass showing different linkages of single [BO₃]/[BO₄] surrounded by Si, Al or Zr polyhedra. (Top row: [BO₃]/[BO₄] surrounded by [SiO₄], second row: [BO₃]/[BO₄] surrounded by [SiO₄] and [ZrO₆], third row: [BO₃]/[BO₄] surrounded by [SiO₄] and [AlO₄], bottom row: [BO₃]/[BO₄] surrounded by [SiO₄], [AlO₄], and [ZrO₆].) Zr, blue octahedra; Si, yellow tetrahedra; B, green triangles (³B) and green tetrahedral (⁴B); Al, red tetrahedral; O, small grey balls; Na, purple crosses; Ca, green crosses

shell was therefore higher and its good agreement with those of the ISG spectra confirmed that the second shell peaks were not simply the result of truncation ripples in the FT.

Dynamic properties

The mean square displacements (MSDs) were calculated from NVE trajectories to analyze diffusion behaviors of ions in simulated glasses, and plots of MSDs of Na and Al from 2Zr glass (ISG) at different temperatures are shown in Fig. 7. MSD plot can be classified into three regions: a ballistic region for short time

(proportional to t^2), a plateau region and a diffusion region for long time (proportional to t).^{28,51,59} The last diffusion region (80–100 ps) was used to calculate the self-diffusion coefficients based on Einstein's equation. In Fig. 7, diffusion regions of Na in both high temperature range (2500–3700 K) and low temperature range (940–1750 K) are proportional to t , while MSD of Al for long time in low temperature range is still the plateau region. Therefore, no diffusion behavior was considered for Al in low temperature range and similar behaviors were observed for Si, B, O, Zr, and Ca. Diffusion coefficients of B, Ca, Na, Al, Zr, and Si in 2Zr (ISG) glass calculated at each temperature are plotted in Fig. 8.

The activation energy barriers of ions in simulated glasses in different temperature ranges calculated based on Arrhenius relationship are listed in Table 5. B, Si, Ca, Al, and Zr ions are considered immobile in low temperature range. Interestingly, E_a of Na in 2Zr (ISG) has a maximum value of 0.50 eV among all glasses in low temperature range (940–1450 K), while in high temperature range (2500–3700 K), E_a of Na has a minimum value of 0.93 eV. B, Si, and Al in 3Zr glass have a maximum value of 1.76, 1.98, and 1.80 eV among all compositions in high temperature, respectively. E_a of Ca ions increases from 1.29 to 1.38 eV, while E_a of Zr ions decreases from 1.92 to 1.83 eV with increasing ZrO₂/SiO₂ substitution; however, the standard deviations make the trend unclear. It was found experimentally that ²²Na self-diffusion activation energy ranges between 76 to 96 kJ/mol (0.79–1.0 eV, respectively) at 250 to 500 °C in sodium borosilicate glasses depending on the compositions.⁵²

DISCUSSION

Bond lengths of Si–O, [³B–O], [⁴B–O], Al–O, and Zr–O are 1.61, 1.46, 1.55, 1.78, and 2.10 Å, respectively, which are all in good agreement with experimental values. There is no noticeable change on bond distance of each cation–oxygen pair between compositions. N₄ of boron for ISG is ~60% from MD simulation and ~52%³⁷ or ~58%¹⁴ from NMR. Q_n of Si for ISG obtained from NMR has the highest percentage of Q₃ with some of Q₂ and Q₄,⁶ which is lower than MD results (~85% of Q₄) when Si, Al, B, and Zr are all considered as formers. On the other hand, if Si is considered as the only network former, Q₂ (~35%) and Q₃ (~31%) species are dominant in the glass structure. This observation is consistent with Raman spectra study by Mendoza et al.,¹⁶ where Q₄(2T) species ([SiO₄] connects with two [SiO₄] and two other network-former polyhedra) contributed to the strongest peak in the Q_n band between 850 to 1200 cm⁻¹. However, Q_n of Si from NMR is still higher as compared to Q_n from MD when only Si is considered as network former. Better deconvolution of ²⁹Si NMR spectrum could improve the comparison with MD results, for the benefit of glass structural interpretation and potential development for MD simulation.

Bond angles of O–Si–O and O–Al–O are at ~108° and ~107° for all compositions, respectively, indicating both Si and Al are in tetrahedral sites. BAD of O–B–O has a peak and a shoulder contributed by O–³B–O and O–⁴B–O at 119° and 109°, respectively. BAD of O–Zr–O has a highest peak at ~88° and a secondary peak at ~170°, suggesting a slightly distorted octahedral site. This slightly distorted [ZrO₆] octahedral are consistent with experimental observations.^{44–46} BAD of O–Na–O shows a higher/sharper peak at ~60° and a lower/broader peak at ~110° for all compositions, which is consistent with a previous study on soda-lime silicate glasses.⁵³ Interestingly, BADs of O–Ca–O exhibit higher intensity of the peak ~60° as compared to the peak ~90°. This feature is distinctive with previous observations on the glass systems without boron content, where the peak at ~90° of BAD of O–Ca–O has a higher intensity.³⁴ According to a study by Xiang and Du,³⁴ the bonds between BO and Na/Ca (BO–Na/Ca–BO) are responsible for the peak at ~60°, where Na/Ca ions are coordinated to the oxygen ions belonging to the same tetrahedron. The bonds between NBO and Na/Ca

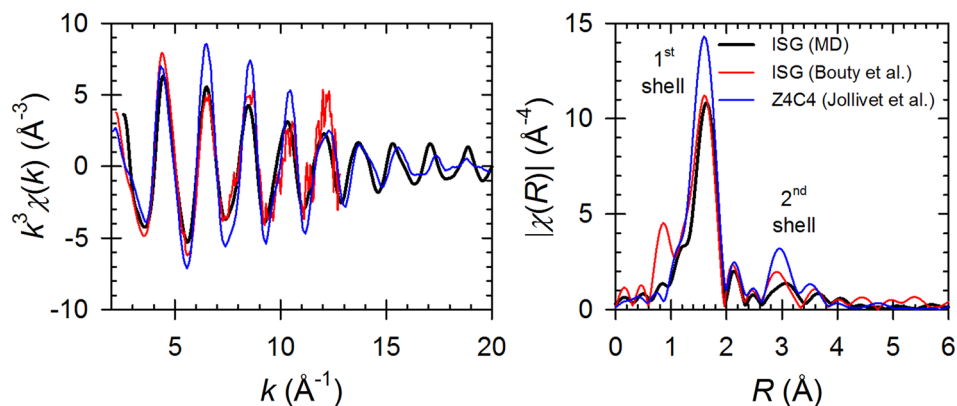


Fig. 6 Experimental and calculated ($\Delta E_0 = 10$ eV) Zr K-edge EXAFS spectra (left) and corresponding Fourier transform magnitudes (right) for Zr in ISG (300 K) or Z4C4 (35 K)

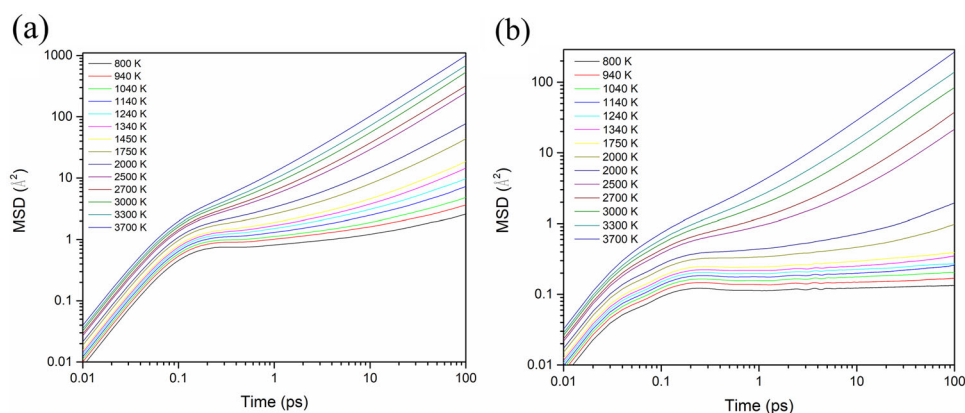


Fig. 7 Mean square displacements (MSDs) of Na (a) and Al (b) in the simulated 2Zr glass (ISG) at different temperatures

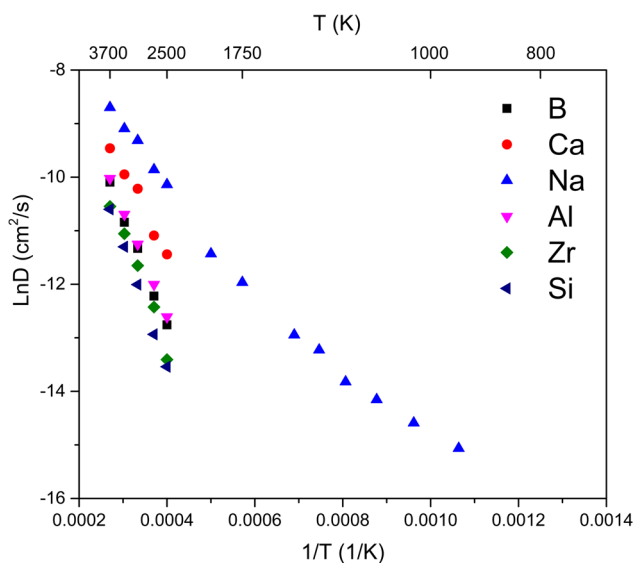


Fig. 8 Self-diffusion coefficients of B, Ca, Na, Al, Zr, and Si in 2Zr glass (ISG) at different temperatures

(NBO-Na/Ca-NBO) are responsible for the peak at higher degree. This observation suggests that Ca ions act more as charge compensators instead of breaking BO in these studied glasses. In this case, less ion exchange sites are available when glasses encounter water molecules, according to a study by Bunker et al.⁵²

where modifiers connected to NBO have a higher tendency to involve in glass dissolution.

Due to the higher cation field strength of Ca^{2+} as compared to Na^+ , it will be intriguing to investigate their role as charge compensators to network former groups such as $[\text{BO}_4]^-$, $[\text{AlO}_4]^-$ and $[\text{ZrO}_6]^{2-}$. CNs of former-Na pairs are always higher than the CNs of former-Ca pairs. For instance, ~80% of charge of $[\text{ZrO}_6]^{2-}$ octahedra are compensated by Na from the comparison of CNs between Zr–Na and Zr–Ca pairs, which is consistent with NMR results.^{42,54} Raman spectroscopy was also used to study the effect of charge compensation of Ca and Na in aluminosilicate glasses.⁵⁵ If we take into consideration that there are higher concentration of Na_2O (12.7 mol%) than CaO (5.7 mol%) in each glass composition, Zr actually has slightly higher preference for Ca as reflected in the preferential distribution analysis (Table 3). This was also supported by higher intensity of Zr–Ca pair distribution as compared to that of Zr–Na pair distribution.³⁷ This preferential behavior of Ca around Zr was also proposed earlier by Calas et al.⁴⁵ Similar situation was observed for ^{41}B and Al. On the other hand, Si prefers Na over Ca even after elimination of compositional effect.

The study of Zr in both simplified and simulant borosilicate glasses using EXAFS^{44,57,60,61} dates back to the late 1990s and has consistently shown that Zr is in 6-fold coordination, with evidence for 7-fold coordinated Zr only appearing at very high ZrO_2 contents.⁶¹ In contrast, the composition of the second shell has not been unequivocally resolved from EXAFS due in large part to the large number of degrees of freedom (elements, distances, coordination numbers, Debye–Waller factors) in the traditional shell-by-shell EXAFS fitting approach. Early attempts to fit the

Table 5. Activation energy of self-diffusion of ions in 0Zr, 2Zr, 3Zr, and 4Zr

E _a (eV)	2500–3700 K						940–1450 K
	B	Si	Ca	Na	Al	Zr	Na
0Zr	1.72 ± 0.04	1.94 ± 0.01	1.29 ± 0.02	0.96 ± 0.01	1.76 ± 0.04	–	0.46 ± 0.02
2Zr	1.73 ± 0.02	1.97 ± 0.04	1.33 ± 0.04	0.93 ± 0.00	1.74 ± 0.04	1.92 ± 0.04	0.50 ± 0.01
3Zr	1.76 ± 0.01	1.98 ± 0.04	1.35 ± 0.10	0.97 ± 0.01	1.80 ± 0.06	1.92 ± 0.08	0.46 ± 0.02
4Zr	1.70 ± 0.02	1.94 ± 0.03	1.38 ± 0.06	0.97 ± 0.01	1.77 ± 0.07	1.83 ± 0.02	0.48 ± 0.01

Standard deviation was obtained from six parallel tests

second shell either failed⁶¹ or had to assume its composition.⁴⁴ More recently, high-resolution data obtained by Jollivet et al.⁵⁸ suggested that the second shell was composed of 4 Si and 2 B with 2.4 Na as the charge compensating species, but other fits were statistically equivalent. Similar results were obtained for ISG by Bouty et al.,⁵⁷ who used empirical potential structural refinement to constrain their fits, but with a greater amount of Na (3.1) as the charge compensating species.

The good agreement between the calculated and experimental Zr K-edge EXAFS spectra not only serves to validate the model employed in this work but also helps resolve the composition of the second shell. The MD simulations show that the second coordination shell around Zr is composed on average of 3.6 Si, 1.9 B, and 0.4 Al with 3.4 Na and 0.9 Ca as the charge compensating species. Because this composition results from MD simulations that are independent of the EXAFS measurements and is therefore not a fit, it does not suffer from the issue encountered in previous work with non-unique solutions.

Network connectivity was successfully used to predict degradation and bioactivity of glasses containing mainly single network former, where the higher NC leads to lower dissolution and bioactivity.^{62,63} However, complications exist for prediction of dissolution for glass systems with multiple network formers such as ISG. Although overall NC from MD increases from 3.76 to 3.83 (by 1.86%) for 0Zr to 4Zr, this solely could not explain the dramatic decrease (higher than 50%) of initial dissolution rate after addition of 1 mol% ZrO₂ from a study by Cailleteau et al.⁴³ Due to different hydrolysis rates⁶⁴ and reaction energies⁶⁵ of different linkages between network formers, many factors such as ^{[3]B} to ^{[4]B} ratio and polyhedra linkages impact the glass dissolution under different environments. Therefore, systematical and statistical analyses from MD provide a better prediction of glass dissolution from compositional and structural information. For instance, hydrolysis rate of ^{[4]B} bonds is smaller than ^{[3]B} bonds according to a study by Yu and Edén.⁶⁴ From our simulation results, even though overall CN of B–Si is decreasing due to the substitution of ZrO₂/SiO₂, CN of ^{[4]B}–Si decreases slower as compared to ^{[3]B}–Si, resulting in less hydrolysis sites available during glass dissolution. Future systematically study on the reaction energies of different linkages under various environments would greatly benefit the prediction of glass dissolution in combination with MD structural study.

In contrast to the generally accepted assumption that boron is not retained at all in alteration layers, Gin et al.³⁷ detected small amounts of boron (~0.4 at%) in the “gel” layer. From the direct observation of glass structure generated by MD simulation, ^{[3]B}/^{[4]B} surrounded by Si, Al or Zr without connecting to another ^{[3]B}/^{[4]B}, as shown in Fig. 5, might contribute to this experimental observation. Further statistical analysis is needed to validity this hypothesis.

From our diffusion analysis, two distinctive trends are observed for Na ions between high and low temperature range, which are divided by glass transition temperature (*T_g*). Note that *T_g* obtained from MD simulation is generally higher than the experimental

values owing to the faster cooling rate used in simulation. From a recent study on cooling rate effect, glass transition temperature decreases with decreasing cooling rate.⁶⁶ After fitting the *T_g* versus cooling rate curve using Vogel–Fulcher dependence of relaxation time, it was found that extrapolation to the experimental cooling rate from the MD simulations can give a reasonable prediction of the *T_g* measured experimentally.⁶⁶ *E_a* of Na in 2Zr (ISG) has a maximum value of 0.50 eV among all glasses in low temperature range, while *E_a* has a minimum value of 0.93 eV in high temperature range. From a study by Bunker et al.,⁵² the results showed that self-diffusion has no effect on the leaching of Na. In high temperature range, B, Si, and Al in 3Zr glass have a maximum value of 1.76, 1.98 and 1.80 eV among all compositions, respectively. Further investigations are required for whether mixed-former effect exists and the relationship between self-diffusion and dissolution behavior.

Radiation would modify nuclear waste glass structure and properties. It has been shown experimentally and from simulations that radiation induces swelling of the samples and change of mechanical properties of nuclear waste glasses.⁶⁷ These modifications of macroscopic properties are originated from changes of medium range glass structures as a result of increasing disorder and increase of internal energy due to irradiation.⁶⁷ These structural changes would also impact the reaction of glass water and dissolution behaviors that demand further simulation and experimental studies.

In summary, ZrO₂/SiO₂ substitution increases the glass network connectivity due to the 6-coordinated [ZrO₆] octahedra, which is consistent with the experimental observations on increased glass transition temperature and lowered thermal expansion coefficient. Basic glass structural features such as bond lengths of cation–oxygen and cation–cation pairs, and BAD of oxygen–cation–oxygen are not sensitive to ZrO₂/SiO₂ substitution. Thus, the polyhedra linkages and glass modifiers seem to have great impacts on the initial dissolution rate here. For a constant CaO and Na₂O content, ZrO₂/SiO₂ substitution leads to a greater proportion of Ca²⁺ and Na⁺ ions serving as charge compensating species, resulting in fewer modifiers available to create NBOs. Modifiers act as charge compensators have a lower tendency to be involved in ion-exchange reaction compared to the modifiers connected with NBOs. Fewer ion-exchange and hydrolysis sites are therefore available during glass dissolution as a result of ZrO₂/SiO₂ substitution. Importantly, ring size analysis revealed that the addition of ZrO₂ tightens the glass network by forming smaller rings, which restrain the water access to both ion-exchange and hydrolysis sites. The calculated EXAFS spectra provide more information than traditional shell-by-shell fitting, which opens the door to characterization of local structural environment around Zr and other glass components.

Methodology

Glass compositions and MD simulation details. Compositions studied and density calculated by a method developed by Fluegel⁶⁸ are listed in Table 6, where 0Zr, 2Zr (ISG), 3Zr, and 4Zr

represent different molar percentages of ZrO₂ substitution of SiO₂ in each glass composition.

The interatomic interactions are described by the Born model of solids using partial charge pairwise potentials and the covalent character of the bond (e.g. Si–O) is described by the partial charge on the ions. The interatomic potential energy $\Phi(r_{ij})$ consists of long-range Coulombic interactions and short-range interactions in the Buckingham form:

$$\Phi(r_{ij}) = \frac{q_i q_j}{r_{ij}} + A_{ij} e^{-\frac{r_{ij}}{\rho_{ij}}} - \frac{C_{ij}}{r_{ij}^6} \quad (2)$$

where r_{ij} is the interatomic distance between atom i and j ; q_i and q_j are the effective charge for atom i and j , respectively, A_{ij} , ρ_{ij} , and C_{ij} are the parameters for the Buckingham term. Detailed description of the potential for borosilicate can be found in our previous study.³⁶ Atomic charges and Buckingham potential parameters used in this work are shown in Table 7. All simulation cells were in cubic shape. Total numbers of atoms in the simulation cells for structural analysis and diffusion analysis were ~24000 and ~12000, respectively.

MD simulations were performed with DL_POLY 2.20 program developed at Daresbury Laboratory in the UK.⁶⁹ Three random configurations for each composition were generated and simulated through a melt-quench process. The initial atom positions were generated randomly with calculated density in a cubic simulation box. After initial relaxation at 300 K under zero pressure, the glasses were melted at 6000 K and the temperature was gradually reduced with a cooling rate of ~1.4 K/ps. At each temperature, the system was run under canonical ensemble

(constant number, volume and temperature (NVT)) for 200 picosecond (ps), which was followed by equilibration under microcanonical ensemble (constant number, volume, and energy (NVE)) for another 200 ps. At 300 K, the trajectory was recorded every 50 steps of the last 40,000 steps under NVE ensemble for final structural analysis. The cutoff distance used for the short-range interactions was 8 Å, and 10 Å for the real-space sum of the electrostatic interactions, which were calculated using the Ewald sum method with a relative precision of 1×10^{-6} . Integration of motion equations was carried out using the Verlet Leapfrog algorithm with a time step of 1 femtosecond (fs).

Structural and dynamical analyses. All the cutoff distances of first/second coordination shell for coordination calculations and BAD analysis are presented in Table 8. The cutoff values were obtained as the first minimum from partial correlation functions.

In the network structure analysis, SiO₂, B₂O₃, Al₂O₃, and ZrO₂ are all considered as glass network formers. Network connectivity (NC) was calculated based on the Q_n distribution of Si⁴⁺, B³⁺, Al³⁺, and Zr⁴⁺ species analyzed from the structures calculated from MD simulations through the following equation (3):

$$NC = \frac{\sum_{n=0}^4 n \times Q_n^{Si} \times [SiO_2] + \sum_{n=0}^4 n \times Q_n^B \times [BO_{3/2}] + \sum_{n=0}^4 n \times Q_n^{Al} \times [AlO_{3/2}] + \sum_{n=0}^6 n \times Q_n^{Zr} \times [ZrO_2]}{[SiO_2] + [BO_{3/2}] + [AlO_{3/2}] + [ZrO_2]} \quad (3)$$

where n is the number of the bridging-oxygen atoms per unit and Q_n^{Si} is the fraction of Si atoms in Si–Q–X linkages where X is one of the four network former cations, $\sum n \times Q_n^{Si}$ is then the network connectivity of Si (NC_{Si}) and $[SiO_2]$ is the mol% of SiO₂ in the glass composition, as well as for B, Al, and Zr.

The glass structures generated from the melt-quench process mentioned above were used for diffusion calculations. Six random configurations for each composition were simulated in order to obtain a reasonable standard deviation. The glasses were gradually heated from 300 to 3700 K with intervals of 800, 940, 1040, 1140, 1240, 1340, 1450, 1750, 2000, 2500, 2700, 3000, and 3300 K. At each temperature, the glasses were first equilibrated for 60 ps under NVT ensemble and then run under NVE for 200 ps, within which the trajectory was recorded in the last 180 ps every 10 fs for diffusion analysis. The MSDs were calculated from these trajectories, based on which the self-diffusion coefficients were obtained using Einstein's equation,

$$D = \frac{1}{6} \lim_{t \rightarrow \infty} \frac{\langle r^2 \rangle}{t} \quad (4)$$

where $\langle r^2 \rangle$ is MSD and t is time. The diffusion activation energy barriers were then calculated from diffusion coefficient at different temperatures by taking the logarithm on Arrhenius equation,

$$D = D_0 \exp\left(\frac{-E_a}{RT}\right) \quad (5)$$

where E_a is the diffusion energy barrier, T is the temperature and R is the gas constant. Details of calculations can be found in a study by Ren and Du.⁵⁹

EXAFS spectra calculations. A configuration was collected every 0.5 ps for the last 11 ps of the 300 K NVE production run. For each

Glass	Composition (mol %)						Density (g/cm ³) ⁶⁸
	Na ₂ O	CaO	Al ₂ O ₃	B ₂ O ₃	ZrO ₂	SiO ₂	
0Zr	12.6	5.7	3.8	16.0	–	61.9	2.4641
2Zr (ISG)	12.6	5.7	3.8	16.0	1.7	60.2	2.4980
3Zr	12.6	5.7	3.8	16.0	3.0	58.9	2.5209
4Zr	12.6	5.7	3.8	16.0	4.0	57.9	2.5370

Pair	A (eV)	ρ (Å)	C (eV Å ⁶)
Si ^{2.4} –O ^{−1.2}	13,702.9050	0.193817	54.681
Na ^{0.6} –O ^{−1.2}	4383.7555	0.243838	30.700
Ca ^{1.2} –O ^{−1.2}	7747.1834	0.252623	93.109
B ^{1.8} –O ^{−1.2}	14,912.9675 ^a	0.171281	28.500
Al ^{1.8} –O ^{−1.2}	12,201.4170	0.195628	31.997
Zr ^{2.4} –O ^{−1.2}	17,943.3840	0.226627	127.650
O ^{−1.2} –O ^{−1.2}	2029.2204	0.343645	192.580

^aA value is for 2Zr (ISG). A value for 0Zr, 3Zr, and 4Zr is 14,734.6070, 15,244.7217 and 15,152.5909, respectively

Pair/cutoff	Pair/cutoff	Pair/cutoff	Pair/cutoff	Pair/cutoff	Pair/cutoff
Si–O/2.25	Si–B/3.33	Si–Al/4.11	Si–Zr/4.09	Si–Na/4.43	Si–Ca/4.30
B–O/1.85	B–Al/3.48	B–Zr/4.08	B–Na/4.26	B–Ca/4.10	B–B/3.25
Al–O/2.50	Al–Zr/4.11	Al–Na/4.56	Al–Ca/4.59	Ca–O/3.14	Na–O/3.16
Zr–O/2.51	Zr–Na/5.17	Zr–Ca/5.10	Zr–Zr/4.39		

configuration, a cluster with a radius of 10 Å centered around each of the Zr ions in the configuration was excised to calculate all the scattering paths with effective distances less than the cluster radius for a Zr K-shell core hole using FEFF9.^{70–72} The S_0^2 parameter calculated by FEFF9 was 0.928 and was used in all calculations. The individual EXAFS spectra thus calculated (1364, 2376, 3168 for 2Zr, 3Zr, and 4Zr, respectively) were averaged for comparison with experimental spectra. The Fourier transform (FT) was applied to the averaged EXAFS spectra using IFEFFIT⁷³ with k^3 weight in the range $2.6 \leq k \leq 12.2 \text{ \AA}^{-1}$ and truncated using a Hanning window with $dk = 1.0 \text{ \AA}^{-1}$ to match the FT parameters used by Bouty et al.⁵⁷

Data availability

The authors declare that all data supporting the findings of this study are available within the paper and its supplementary information files.

ACKNOWLEDGEMENTS

Computational resources were provided by UNT's High Performance Computing Services, a division of the University Information Technology with additional support from UNT Office of Research and Economic Development. We also acknowledge Dr. Olivier Bouty (CEA) for providing experimental X-ray structure factor data and the experimental Zr K-edge spectrum of ISG and helpful discussions with Dr. Stephane Gin (CEA), Dr. Joseph V. Ryan (PNNL), and Dr. John D. Vienna (PNNL). We gratefully acknowledge financial support by the Center for Performance and Design of Nuclear Waste Forms and Containers, an Energy Frontier Research Center funded by the U.S. Department of Energy, Office of Science, Basic Energy Sciences under Award # DE-SC0016584.

AUTHOR CONTRIBUTIONS

X.L. conducted MD simulation, data analysis and manuscript preparation. L.D. contributed to potential development, data analysis, and manuscript preparation. S.K. performed the EXAFS calculations and manuscript preparation. J.D. contributed to simulation design, directing data analysis, and manuscript preparation.

ADDITIONAL INFORMATION

Supplementary information accompanies the paper on the *npj Materials Degradation* website (<https://doi.org/10.1038/s41529-018-0041-6>).

Competing interests: The authors declare no competing interests.

Publisher's note: Springer Nature remains neutral with regard to jurisdictional claims in published maps and institutional affiliations.

REFERENCES

- Calas, G., Cormier, L., Galois, L. & Jollivet, P. Structure–property relationships in multicomponent oxide glasses. *Comptes Rendus Chim.* **5**, 831–843 (2002).
- Gin, S., Frugier, P., Jollivet, P., Bruguiere, F. & Curti, E. New insight into the residual rate of borosilicate glasses: effect of S/V and glass composition. *Int. J. Appl. Glas. Sci.* **4**, 371–382 (2013).
- Inagaki, Y., Kikunaga, T., Idemitsu, K. & Arima, T. Initial dissolution rate of the international simple glass as a function of pH and temperature measured using microchannel flow-through test method. *Int. J. Appl. Glas. Sci.* **4**, 317–327 (2013).
- Gin, S. et al. An international initiative on long-term behavior of high-level nuclear waste glass. *Mater. Today* **16**, 243–248 (2013).
- Inagaki, Y. Micro-channel as a new tool to investigate glass dissolution kinetics. *Procedia Mater. Sci.* **7**, 172–178 (2014).
- Gin, S. et al. Origin and consequences of silicate glass passivation by surface layers. *Nat. Commun.* **6**, 6360 (2015).
- Gin, S. et al. The fate of silicon during glass corrosion under alkaline conditions: A mechanistic and kinetic study with the International Simple Glass. *Geochim. Cosmochim. Acta* **151**, 68–85 (2015).
- Aréna, H. et al. Impact of iron and magnesium on glass alteration: characterization of the secondary phases and determination of their solubility constants. *Appl. Geochem.* **82**, 119–133 (2017).

- Elia, A., Ferrand, K. & Lemmens, K. Determination of the forward dissolution rate for international simple glass in alkaline solutions. *MRS Adv.* **12**, 661–667 (2017).
- Fournier, M., Gin, S. & Frugier, P. Resumption of nuclear glass alteration: state of the art. *J. Nucl. Mater.* **448**, 348–363 (2014).
- Reiser, J. et al. Glass corrosion in the presence of iron-bearing materials and potential corrosion suppressors. *MRS Online Proc. Libr.* **1744**, 139–144 (2015).
- Abdelouas, A. et al. A preliminary investigation of the ISG glass vapor hydration. *Int. J. Appl. Glas. Sci.* **4**, 307–316 (2013).
- Gong, Y., Wren, A. W. & Mellott, N. P. Quantitative morphological and compositional evaluation of laboratory prepared aluminoborosilicate glass surfaces. *Appl. Surf. Sci.* **324**, 594–604 (2015).
- Charpentier, T. et al. Self-healing capacity of nuclear glass observed by NMR spectroscopy. *Sci. Rep.* **6**, 25499 (2016).
- Mendoza, C., Peugeot, S., Bouty, O., Caraballo, R. & Jegou, C. Simplified nuclear glasses structure behaviour under various irradiation conditions: a Raman Spectroscopy Study. *Procedia Chem.* **7**, 581–586 (2012).
- Mendoza, C. et al. Oxide glass structure evolution under swift heavy ion irradiation. *Nucl. Instrum. Methods Phys. Res. Sect. B* **325**, 54–65 (2014).
- Peugeot, S. et al. Alpha decays impact on nuclear glass structure. *Procedia Mater. Sci.* **7**, 252–261 (2014).
- Karakurt, G. et al. Understanding of the mechanical and structural changes induced by alpha particles and heavy ions in the French simulated nuclear waste glass. *J. Nucl. Mater.* **475**, 243–254 (2016).
- Mohd Fadzil, S. et al. Liquidus temperature and chemical durability of selected glasses to immobilize rare earth oxides waste. *J. Nucl. Mater.* **465**, 657–663 (2015).
- Hopf, J. & Pierce, E. M. Topography and mechanical property mapping of International Simple Glass surfaces with atomic force microscopy. *Procedia Mater. Sci.* **7**, 216–222 (2014).
- Guerette, M. & Huang, L. In-situ Raman and Brillouin light scattering study of the international simple glass in response to temperature and pressure. *J. Non Cryst. Solids* **411**, 101–105 (2015).
- Weaver, J. L., Reiser, J., Neill, O. K., McCloy, J. S. & Wall, N. A. A sampling method for semi-quantitative and quantitative electron microprobe analysis of glass surfaces. *MRS Online Proc. Libr.* **1744**, 101–106 (2015).
- Reiser, J. T. et al. The use of positrons to survey alteration layers on synthetic nuclear waste glasses. *J. Nucl. Mater.* **490**, 75–84 (2017).
- Gin, S. et al. Atom-Probe Tomography, TEM and ToF-SIMS study of borosilicate glass alteration rim: A multiscale approach to investigating rate-limiting mechanisms. *Geochim. Cosmochim. Acta* **202**, 57–76 (2017).
- Du, J. Challenges in molecular dynamics simulations of multicomponent oxide glasses. in *Molecular Dynamics Simulations of Disordered Materials* (eds. Massobrio, C., Du, J., Bernasconi, M. & Salmon, P. S.) **215**, 157–180 (Springer International Publishing, Switzerland, 2015).
- Du, J. & Cormack, A. N. The medium range structure of sodium silicate glasses: a molecular dynamics simulation. *J. Non Cryst. Solids* **349**, 66–79 (2004).
- Xiang, Y., Du, J., Smedskjaer, M. M. & Mauro, J. C. Structure and properties of sodium aluminosilicate glasses from molecular dynamics simulations. *J. Chem. Phys.* **139**, 44507 (2013).
- Du, J. & Corrales, L. R. Structure, dynamics, and electronic properties of lithium disilicate melt and glass. *J. Chem. Phys.* **114702**, 114702 (2006).
- Kokou, L. & Du, J. Short- and medium-range structures of cerium aluminophosphate glasses: a molecular dynamics study. *J. Non Cryst. Solids* **403**, 67–79 (2014).
- Kokou, L. & Du, J. Rare earth ion clustering behavior in europium doped silicate glasses: simulation size and glass structure effect. *J. Non Cryst. Solids* **358**, 3408–3417 (2012).
- Du, J. & Kokou, L. Europium environment and clustering in europium doped silica and sodium silicate glasses. *J. Non Cryst. Solids* **357**, 2235–2240 (2011).
- Du, J. & Cormack, A. N. The structure of erbium doped sodium silicate glasses. *J. Non Cryst. Solids* **351**, 2263–2276 (2005).
- Brogli, G., Mugoni, C., Du, J., Siligardi, C. & Montorsi, M. Lithium vanadophosphate glasses: structure and dynamics properties studied by molecular dynamics simulations. *J. Non Cryst. Solids* **403**, 53–61 (2014).
- Xiang, Y. & Du, J. Effect of strontium substitution on the structure of 4555 Bio-glasses. *Chem. Mater.* **23**, 2703–2717 (2011).
- Du, J. & Xiang, Y. Effect of strontium substitution on the structure, ionic diffusion and dynamic properties of 4555 bioactive glasses. *J. Non Cryst. Solids* **358**, 1059–1071 (2012).
- Lu, X. et al. Effects of boron oxide substitution on the structure and bioactivity of SrO-containing bioactive glasses. *J. Mater. Sci.* **52**, 8793–8811 (2017).
- Collin, M. et al. Structure of international simple glass and properties of passivating layer formed in circumneutral pH conditions. *npj Mater. Degrad.* **2**, 4 (2018).
- Karell, R., Kraxner, J. & Chromčíková, M. Properties of selected zirconia containing silicate glasses. *Ceram. - Silik.* **50**, 78–82 (2006).

39. Fisher, J. G., James, P. F. & Parker, J. M. Soda lime zirconia silicate glasses as prospective hosts for zirconia-containing radioactive wastes. *J. Non Cryst. Solids* **351**, 623–631 (2005).
40. Nkurunziza, G., Debaiky, A., Cousin, P. & Benmokrane, B. Durability of GFRP bars: a critical review of the literature. *Prog. Struct. Eng. Mater.* **7**, 194–209 (2005).
41. Cailleteau, C. et al. Insight into silicate-glass corrosion mechanisms. *Nat. Mater.* **7**, 978–983 (2008).
42. Bergeron, B. et al. First investigations of the influence of IVB elements (Ti, Zr, and Hf) on the chemical durability of soda-lime borosilicate glasses. *J. Non Cryst. Solids* **356**, 2315–2322 (2010).
43. Cailleteau, C. C., Devreux, F. F., Spalla, O., Angeli, F. F. & Gin, S. S. Why do certain glasses with a high dissolution rate undergo a low degree of corrosion? *J. Phys. Chem. C* **115**, 5846–5855 (2011).
44. Galois, L. et al. Evidence for 6-coordinated zirconium in inactive nuclear waste glasses. *J. Am. Ceram. Soc.* **82**, 2219–2224 (1999).
45. Calas, G., Galois, L., Cormier, L., Ferlat, G. & Lelong, G. The structural properties of cations in nuclear glasses. *Procedia Mater. Sci.* **7**, 23–31 (2014).
46. Ferlat, G. et al. Evidence for symmetric cationic sites in zirconium-bearing oxide glasses. *Phys. Rev. B* **73**, 214207 (2006).
47. Montorsi, M., Leonelli, C., Menziani, M. C., Du, J. & Cormack, A. N. Molecular dynamics study of zirconia containing glasses. *Phys. Chem. Glas.* **43**, 137–142 (2002).
48. Du, J., Devanathan, R., Corrales, L. R., Weber, W. J. & Cormack, A. N. Short- and medium-range structure of amorphous zircon from molecular dynamics simulations. *Phys. Rev. B* **74**, 214204 (2006).
49. Connelly, A. J., Travis, K. P., Hand, R. J., Hyatt, N. C. & Maddrell, E. Composition-structure relationships in simplified nuclear waste glasses: 2. the effect of ZrO₂ additions. *J. Am. Ceram. Soc.* **94**, 137–144 (2011).
50. Du, J. & Xiang, Y. Investigating the structure–diffusion–bioactivity relationship of strontium containing bioactive glasses using molecular dynamics based computer simulations. *J. Non Cryst. Solids* **432**, 35–40 (2016).
51. Han, X. J. & Schober, H. R. Transport properties and Stokes-Einstein relation in a computer-simulated glass-forming Cu_{33.3}Zr_{66.7} melt. *Phys. Rev. B* **83**, 224201 (2011).
52. Bunker, B. C., Arnold, G. W., Day, D. E. & Bray, P. J. The effect of molecular structure on borosilicate glass leaching. *J. Non Cryst. Solids* **87**, 226–253 (1986).
53. Cormack, A. N. & Du, J. Molecular dynamics simulations of soda-lime-silicate glasses. *J. Non Cryst. Solids* **293–295**, 283–289 (2001).
54. Angeli, F., Charpentier, T., De Ligny, D. & Cailleteau, C. Boron speciation in soda-lime borosilicate glasses containing zirconium. *J. Am. Ceram. Soc.* **93**, 2693–2704 (2010).
55. Hehlen, B. & Neuville, D. R. Raman response of network modifier cations in aluminosilicate glasses. *J. Phys. Chem. B* **119**, 4093–4098 (2015).
56. Tilocca, A., Cormack, A. N., & Leeuw, N. H. De. The structure of bioactive silicate glasses: New insight from molecular dynamics simulations. *Chem. Mater.* **91**, 95–103 (2007).
57. Bouty, O., Cammelli, S. & Solari, P. L. Structural insights for the International Simple Glass by combining X-ray absorption spectroscopic analysis and atomistic modelling. *J. Non. Cryst. Solids* (2017). <https://doi.org/10.1016/j.jnoncrsol.2017.11.013>
58. Jollivet, P. et al. An enhanced resolution of the structural environment of zirconium in borosilicate glasses. *J. Non Cryst. Solids* **381**, 40–47 (2013).
59. Ren, M. & Du, J. Structural origin of the thermal and diffusion behaviors of lithium aluminosilicate crystal polymorphs and glasses. *J. Am. Ceram. Soc.* **99**, 2823–2833 (2016).
60. Connelly, A. J. et al. The structural role of Zr within alkali borosilicate glasses for nuclear waste immobilisation. *J. Non Cryst. Solids* **357**, 1647–1656 (2011).
61. McKeown, D. A. et al. Formulation, testing, and structural characterization of high-zirconium high-level waste glasses. *Mater. Res. Soc. Symp. Proc.* **556**, 305–312 (1999).
62. Hill, R. G. & Brauer, D. S. Predicting the bioactivity of glasses using the network connectivity or split network models. *J. Non Cryst. Solids* **357**, 3884–3887 (2011).
63. Edén, M. The split network analysis for exploring composition–structure correlations in multi-component glasses: I. Rationalizing bioactivity-composition trends of bioglasses. *J. Non Cryst. Solids* **357**, 1595–1602 (2011).
64. Yu, Y. & Edén, M. Structure–composition relationships of bioactive borophosphosilicate glasses probed by multinuclear ¹¹B, ²⁹Si, and ³¹P solid state NMR. *RSC Adv.* **6**, 101288–101303 (2016).
65. Zapol, P., He, H., Kwon, K. D. & Criscenti, L. J. First-principles study of hydrolysis reaction barriers in a sodium borosilicate glass. *Int. J. Appl. Glas. Sci.* **4**, 395–407 (2013).
66. Deng, L. & Du, J. Effects of system size and cooling rate on the structure and properties of sodium borosilicate glasses from molecular dynamics simulations. *J. Chem. Phys.* **148**, 24504 (2018).
67. Delaye, J. M., Peugeot, S., Bureau, G. & Calas, G. Molecular dynamics simulation of radiation damage in glasses. *J. Non Cryst. Solids* **357**, 2763–2768 (2011).
68. Fluegel, A. Global model for calculating room-temperature glass density from the composition. *J. Am. Ceram. Soc.* **90**, 2622–2625 (2007).
69. Smith, W., Foreste, T. R. & Todorov, I. T. The DL POLY2 user manual. (2010).
70. Rehr, J. J. & Albers, R. C. Theoretical approaches to x-ray absorption fine structure. *Rev. Mod. Phys.* **72**, 621–654 (2000).
71. Rehr, J. J. et al. Ab initio theory and calculations of X-ray spectra. *Comptes Rendus Phys.* **10**, 548–559 (2009).
72. Rehr, J. J., Kas, J. J., Vila, F. D., Prange, M. P. & Jorissen, K. Parameter-free calculations of X-ray spectra with FEFF9. *Phys. Chem. Chem. Phys.* **12**, 5503 (2010).
73. Newville, M. IFEFFIT: interactive XAFS analysis and FEFF fitting. *J. Synchrotron Radiat.* **8**, 322–324 (2001).
74. Michel, F. et al. Mechanisms of boron coordination change between borosilicate glasses and melts. *J. Non Cryst. Solids* **379**, 169–176 (2013).
75. Fábrián, M., Sváb, E., Proffen, T. & Veress, E. Structure study of multi-component borosilicate glasses from high-Q neutron diffraction measurement and RMC modeling. *J. Non Cryst. Solids* **354**, 3299–3307 (2008).
76. Cormier, L., Ghaleb, D., Delaye, J.-M. & Calas, G. Competition for charge compensation in borosilicate glasses: wide-angle x-ray scattering and molecular dynamics calculations. *Phys. Rev. B* **61**, 14495–14499 (2000).
77. FitzGerald, V. et al. A neutron and X-ray diffraction study of Bioglass® with reverse Monte Carlo modelling. *Adv. Funct. Mater.* **17**, 3746–3753 (2007).
78. Weigel, C., Cormier, L., Calas, G., Galois, L. & Bowron, D. T. Intermediate-range order in the silicate network glasses NaFe_xAl_{1-x}Si₂O₆ (x=0,0.5,0.8,1): a neutron diffraction and empirical potential structure refinement modeling investigation. *Phys. Rev. B* **78**, 1–11 (2008).
79. Meneghini, C., Gualtieri, A. F. & Siligardi, C. Differential anomalous wide-angle X-ray scattering and X-ray absorption experiments to investigate the formation of glass ceramics in the CaO–SiO₂–ZrO₂ system. *J. Appl. Crystallogr.* **32**, 1090–1099 (1999).
80. McKeown, D. A., Muller, I. S., Buechele, A. C. & Pegg, I. L. X-ray absorption studies of the local environment of Zr in high-zirconia borosilicate glasses. *J. Non Cryst. Solids* **258**, 98–109 (1999).



Open Access This article is licensed under a Creative Commons Attribution 4.0 International License, which permits use, sharing, adaptation, distribution and reproduction in any medium or format, as long as you give appropriate credit to the original author(s) and the source, provide a link to the Creative Commons license, and indicate if changes were made. The images or other third party material in this article are included in the article's Creative Commons license, unless indicated otherwise in a credit line to the material. If material is not included in the article's Creative Commons license and your intended use is not permitted by statutory regulation or exceeds the permitted use, you will need to obtain permission directly from the copyright holder. To view a copy of this license, visit <http://creativecommons.org/licenses/by/4.0/>.

© The Author(s) 2018